Enhanced critical current density of ex situ MgB$_2$ via control of Mg assisted sintering

Nurhidayah Mohd Hapipi[1], Soo Kien Chen[1,2,*] , Abdul Halim Shaari[1], Mohd Mustafa Awang Kechik[1], Kean Pah Lim[1], Kar Ban Tan[3], Oon Jew Lee[4], Sai Srikanth Arvapalli[5], and Muralidhar Miryala[5]

[1] *Department of Physics, Faculty of Science, Universiti Putra Malaysia, 43400 UPM Serdang, Selangor, Malaysia*

[2] *Institute of Advanced Technology, Universiti Putra Malaysia, 43400 UPM Serdang, Selangor, Malaysia*

[3] *Department of Chemistry, Faculty of Science, Universiti Putra Malaysia, 43400 UPM Serdang, Selangor, Malaysia*

[4] *Faculty of Science and Marine Environment, Universiti Malaysia Terengganu, 21030 Kuala Nerus, Terengganu, Malaysia*

[5] *Graduate School of Science and Engineering, Regional Environment Systems, Superconducting Research Laboratory (SRL), Shibaura Institute of Technology, 3-7-5 Toyosu, Koto-ku, Tokyo 135-8548, Japan*

ABSTRACT

In this work, ex situ MgB$_2$ was mixed with 0.5 mol of Mg and sintered. The sintering conditions were varied over a temperature range of 600–1000 °C for 1, 3, and 7 h, respectively. The addition of Mg during the sintering increased the partial pressure of Mg and thus suppressed the decomposition of MgB$_2$. Onset of critical temperature, T_c, was retained at $\sim$ 38 K even after the addition of Mg. By increasing the sintering temperature, magnetic critical current density, J_c at self-field, and 20 K of the ex situ samples increased consistently. With the addition of Mg for 1 h sintering, self-field J_c (20 K) was enhanced more than 20 times to 10^4 A cm^{-2} as the sintering temperature was increased. Such significant enhancement in the J_c is mainly due to the improved grain coupling aided by Mg during the short sintering.

1 Introduction

Magnesium diboride (MgB$_2$) has a high critical temperature, $T_c \sim 40$ K among the non-cuprate based superconductors [1]. Attractive properties of MgB$_2$, such as low anisotropy and transparency of grain boundaries to current flow, make it a promising material for industrial applications [1–3]. From the perspective of conductor and coil development, high field magnets, magnetic resonance imaging, and transmission cables are among the potential usages of MgB$_2$ [4–6]. Like the nano-scale secondary phases in the cuprate superconductors [7, 8], grain boundaries of MgB$_2$ can act as flux pinning centers which are essential for the material to carry high critical current density, J_c [9].

There are two common routes to prepare MgB$_2$, namely in situ [10–13] and ex situ [14–16] methods. For the in situ method, elemental powders of magnesium (Mg) and boron (B) in a molar ratio of 1:2 are

mixed and then subject to heat treatment to form MgB_2. During the heat treatment process, the formation of MgB_2 occurs through a liquid–solid reaction in which Mg grains melt and diffuse into B grains. For the ex situ approach, pre-reacted MgB_2 powder is used as starting precursor for further processing. It is known that the coupling of grains across grain boundaries (grain coupling) for ex situ samples is weaker than that of in situ ones, though the former has a higher packing factor of $\sim$ 75% [3]. Unlike the stronger grain coupling in in situ MgB_2, the pre-reacted ex situ MgB_2 grain aggregates are poorly connected, leading to the reduced effective cross-sectional area for current transport, thus lower J_c [14, 17]. If the grain coupling of the ex situ samples is improved, their J_c should outperform that of the in situ MgB_2.

One effective way to optimize J_c is by varying the heat treatment conditions. Optimum heat treatment can strengthen grain connectivity and reduce oxidation and volatility of Mg, leading to high J_c. For instance, the sintering temperature of the in situ MgB_2 samples was varied from 775 to 805 °C for 3 h [18]. It was found that the J_c (0 T, 20 K) increased to 245 kA/cm^2 for the sample sintered at 805 °C [18]. The increment in J_c was due to the reduction of grain size (up to the nanometer regime), which enhanced flux pinning at the grain boundaries [18].

For ex situ MgB_2 fabricated by powder-in-closed-tube (PICT) method and sintered at 900 °C for 48 h, the packing factor was improved, indicating the presence of a larger intergrain contact area that decreased the resistivity of the samples [3]. Such a self-sintering method is promising for obtaining high connectivity (K > 20%) as a result of improved intergranular coupling strength [14]. It is noteworthy that the normalized flux pinning force plots of the ex situ MgB_2 sintered at 900 °C for 48 h is very close to that of the in situ one implying that they have the same flux pinning mechanism [14]. This is so most probably because the grain size of the ex situ samples is quite similar to that of the in situ ones, as the sintering condition did not promote grain growth of the former [14].

Due to the high volatility of Mg at elevated temperatures, excess Mg during the in situ MgB_2 preparation is essential to compensate for the loss of Mg [19, 20]. It was found that the use of excess Mg led to reduced MgO phase and improved grain connectivity [19, 20]. Consequently, the irreversibility

field, H_{irr}, and J_c were increased [19, 20]. The highest J_c (8 T, 10 K) of 3×10^4 A/cm^2 was obtained for 10 at% Mg excess MgB_2/Fe wires, which were heated at 600 °C for 1 h. The transport J_c at a field up to 14 T for 10 at% Mg excess samples heated at 800 °C for 30 min increased by a factor of two as compared with the similar samples without the addition of excess Mg [19]. Zhang et al. varied the molar percentage of excess Mg addition (0–30 mol%) into in situ MgB_2 [20]. The highest J_c was obtained in the 5 mol% excess Mg sample with the best grain connectivity. It was also found that the sample density increased for excess Mg content up to 5 mol%. However, T_c decreased slightly ($\sim$ 1.5 K) with the addition of excess Mg [17].

For ex situ MgB_2, it was found that the addition of Mg (MgB_2: Mg = 100:10) during the sintering process at 700 °C for 1 h reduced oxidation and thus decreased the weight fraction of MgO in the samples [21]. Apart from this, the density of the samples increased more significantly with the prolonged sintering time. As shown in the scanning electron microscopy images, the Mg added samples showed better grain connectivity, as evidenced by the neck formation among the grains, probably due to accelerated self-sintering. Therefore, the width of superconducting transition, ΔT_c, is smaller for the samples with the addition of Mg, suggesting improved grain coupling compared with the ones without the addition of Mg.

In view of the higher packing factor of ex situ MgB_2 as a lightweight material for conductor development, this work systematically investigates the combined effects of heat treatment conditions and the addition of Mg on T_c and J_c of ex situ MgB_2. As demonstrated previously [14, 21], appropriate heat treatment and addition of Mg are expected to increase J_c of ex situ MgB_2 through enhancement of its grain coupling. Unlike the work reported previously [14], whereby the sintering of ex situ MgB_2 was varied in the range of 700–1000 °C for 3–240 h, we focus on shorter sintering time (1, 3, 7 h) and lower sintering temperature (600 °C, 700 °C, 900 °C). For ex situ MgB_2 added with Mg, samples were prepared according to the stoichiometry of MgB_2 + 0.5 Mg [22]. For this set of samples, we chose 700 °C and 1000 °C as the lower and upper bound temperatures according to the work reported in [14] with a shorter sintering time of 1, 3, and 7 h. The sintering temperature and sintering time were varied in order to find the optimum

condition for improving the grain connectivity, hence the J_c of the samples.

2 Experimental details

Commercially available magnesium diboride, MgB_2 powder (99.0% purity, Alfa Aesar) was used as a starting material (hereafter denoted as ex situ MgB_2). For Mg added samples, 0.5 mol of Mg was added to the ex situ MgB_2 according to the stoichiometry of $MgB_2 + 0.5$ Mg. The mixture was ground for 1 h before being pressed into circular pellets (13 mm diameter and ~ 1 mm thickness) using a hydraulic press under a 5-ton pressure. The same pelletizing procedure was applied to the ex situ MgB_2 powder (without the addition of Mg). Then, the pellets were loaded into stainless steel tubes, and both ends of the tubes were clamped before undergoing heat treatment in argon gas flow to minimize oxidation. The powder handling process was carried out in the air. Sintering of the ex situ MgB_2 was conducted at 600 °C, 700 °C, and 900 °C, respectively, for 1 h. For sintering at 700 °C, sintering time was varied for 1, 3, and 7 h, respectively. For the Mg added ex situ MgB_2 samples, sintering was carried out at 700 °C and 1000 °C for 1, 3, and 7 h, respectively.

Phase formation and crystal structure of the samples were identified by X-ray diffraction (XRD) technique using the PW 3040/60 MPD X'pert Pro Panalytical Philips DY 1861 X-ray diffractometer with Cu-K$_\alpha$ radiation source ($\lambda = 1.5406$ Å). The scanning was carried out in 2θ θ range of 20°–80° with an increment step size of 0.03°. The microstructure of the samples was imaged using a scanning electron microscope (SEM-LEO 1455 VPSEM). The average grain size of the samples was calculated from the randomly selected 100 grains based on the SEM images using the software Image-J. The critical temperature, T_c, and critical current density, J_c, were measured using a SQUID (superconducting quantum interference device) magnetometer (Quantum Design: MPMS5). The samples were zero-field cooled. Magnetization hysteresis (M-H) loops were acquired by measuring the samples in magnetic fields from 0 to $+ 5$ T at 20 K. The fields were applied parallel to the longest dimension of the samples. The J_c of the samples with dimensions of approximately $1.0 \times 1.0 \times 0.5$ mm^3 was calculated from the M-H loops based on the extended Bean's critical state model equation [23]:

$$J_c = 20\Delta m/[a^2 d(b - (a/3))] \tag{1}$$

where d is the sample thickness, a, b ($a < b$) are cross-sectional dimensions of a rectangular sample and Δm (in emu units, 1 emu = 10^{-3} Am^2) is the width of the M-H loop.

3 Results and discussion

3.1 X-ray diffraction (XRD) analysis

Figures 1 and 2 show the XRD patterns of the ex situ MgB_2 samples and that with the addition of Mg sintered with different heat treatment conditions, respectively. Major peaks for all the samples were indexed to MgB_2 with hexagonal crystal structure and $P6/mmm$ space group (ICSD: 98-010-6149). Peak with the highest intensity was observed at $2\theta \approx 42.4°$ that corresponds to the Miller indices (1 0 1) of the MgB_2 phase. Some minor peaks were indexed to MgO (ICSD: 98-009-4096). The presence of MgO is unavoidable since the powder handling process was carried out in the open air. Moreover, air trapped in the stainless steel tubes before sealing the pellets for heat treatment also contained oxygen. Mg is a good
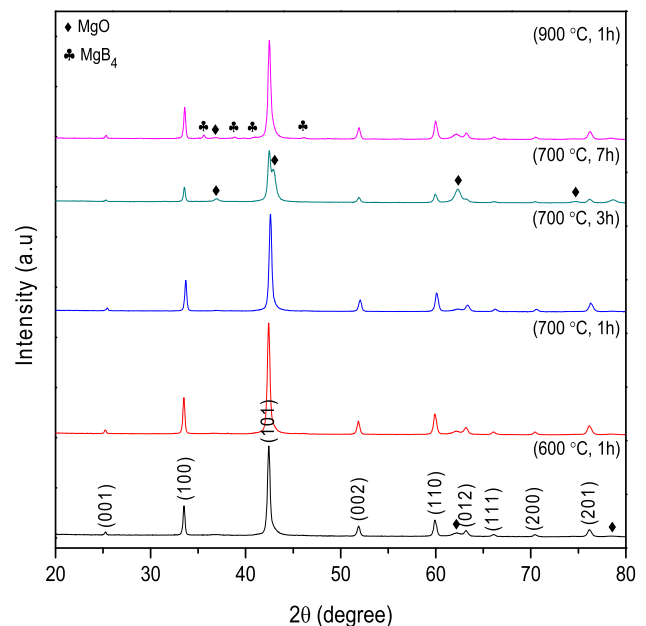

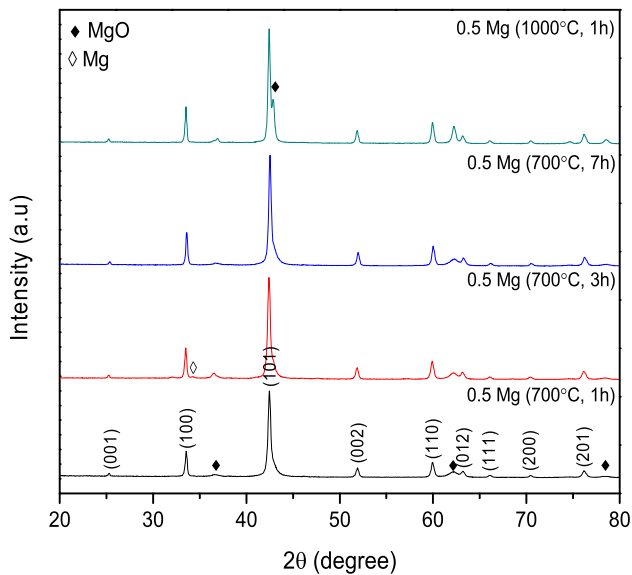**Fig. 1** X-ray diffraction patterns of ex situ MgB_2 samples sintered at different conditions

Fig. 2 X-ray diffraction patterns of 0.5 mol Mg added samples sintered at different conditions

oxygen scrubber that reacts readily with oxygen [10, 24]. Weak peaks indexable to MgB_4 (ICSD: 98-009-1660) started to appear in some of the *ex situ* MgB_2 samples sintered at 700 °C and 900 °C (Fig. 1). The formation of MgB_4 occurred due to the decomposition of MgB_2 [25–27]. However, no MgB_4 peaks were observed for the samples with the addition of Mg (Fig. 2). With the addition of Mg, the increased partial pressure of Mg either prevented or reduced the decomposition rate of MgB_2. Unreacted Mg was also detected in the sample sintered at 700 °C for 3 h.

Tables 1 and 2 show the intensity fraction of the phases formed and lattice parameters of the *a*- and *c*-axis for the ex situ samples with and without Mg addition. The lattice parameters of the *a*- and *c*-axis were obtained by refining the XRD data of the samples via Rietveld analysis using the software HighScore Plus [28]. For the refinement, background fitting was first carried out. Then, phase identification was done by performing the functions "Search Peaks" followed by "Search & Match" to identify all the possible phases from the XRD patterns. Subsequently, the global parameters, scale factor, Caglioti parameters (U, V, W), and peak shape were refined. As the refinement was done progressively, the smaller the goodness of fit (GOF) indicated the better the results. It should be noted that the refinement was undertaken using semi-automatic mode. As shown in Table 1, no specific change trend in the *a*- lattice parameter was observed as the sintering temperature

and time varied. Relative to the ex situ MgB_2 powder before sintering (Unsintered), the most considerable change of the *a*-axis due to the sintering temperature and sintering time is only 0.016% and 0.032%, respectively. Conversely, the change in the *c*-axis with the sintering temperature and sintering time is more remarkable due to the variation of Mg content (due to its high volatility). Such an observation may agree with the previous finding that variation in Mg content predominantly distorts the *c*-axis [29]. Looking at Table 1, the values of the *a*- and *c*-axis are comparable for the samples with a higher and lower amount of MgO and MgB_4, suggesting the negligibly small influence of these phases on the lattice parameters. Intensity fractions of the phases formed were estimated using the formula [30–32]:

$$MgB_2(\%) = \frac{\sum I_{MgB_2}}{\sum I_{MgB_2} + \sum I_{MgO} + \sum I_{Other}} \times 100\% \tag{2}$$

where I is the peak intensity of the phases. The intensity fraction of the MgB_2 phase for the sintered ex situ samples is lower than that of the unsintered powder since the former has a larger MgO fraction and the presence of MgB_4 (Table 1). The increased intensity fraction for the MgB_4 phase with the increasing sintering temperature is associated with the decomposition of MgB_2 into MgB_4 [25, 27, 33]. The decomposition is shown in the chemical reaction below [25]:

$$2MgB_2(s) \rightarrow MgB_4(s) + Mg(g) \tag{3}$$
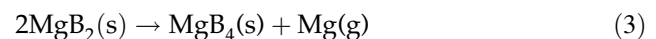
The higher intensity fraction of MgB_4 is consistent with the availability of more Mg vapor for oxidation, forming a higher fraction of MgO in the sample sintered at 900 °C for 1 h [25]. For the samples sintered at 700 °C, prolonged sintering time to 7 h reduced the intensity fraction of the MgB_2 phase to 63.0% (Table 1). The formation of a significantly large fraction of MgO (37.0%) is believed to be due to the longer sintering time of 7 h, thus allowing more sample oxidation to occur. Given the decomposition of MgB_2 into MgB_4 and Mg for the samples sintered at 700 °C for 1 h and 3 h, the same reaction should have also occurred in the sample sintered at 700 °C for 7 h. However, no peak indexable to MgB_4 was observed from the XRD pattern suggesting that part of the Mg vapor had converted MgB_4 to MgB_2 [34, 35]. The source of Mg vapor could be from the

Table 1 Intensity fraction of the phases formed, lattice parameters, and goodness of fit (GOF) for ex situ MgB_2 samples sintered at different conditions

Sintering condition		Intensity fraction (%)			Lattice parameters (Å)		Goodness of Fit (GOF)
Temperature (°C)	Time (h)	MgB_2 (ICSD: 98-010-6149)	MgO (ICSD: 98-009-4096)	MgB_4 (ICSD: 98-009-1660)	a-axis	c-axis	
Unsintered	–	99.6	0.4	–	3.0853 ± 0.0001	3.5226 ± 0.0002	7.43
600	1	97.4	2.6	–	3.0855 ± 0.0001	3.5231 ± 0.0002	3.54
700	1	98.4	1.5	0.1	3.0848 ± 0.0002	3.5231 ± 0.0002	5.27
	3	98.6	1.3	0.1	3.0863 ± 0.0001	3.5250 ± 0.0002	4.52
	7	63.0	37.0	–	3.0851 ± 0.0002	3.5233 ± 0.0003	2.94
900	1	92.9	3.2	3.9	3.0858 ± 0.0002	3.5251 ± 0.0002	4.97

Related data for the unsintered ex situ MgB_2 powder (labeled as Unsintered) is included for comparison

Table 2 Intensity fraction of the phases formed, lattice parameters, and goodness of fit (GOF) for 0.5 mol Mg added ex situ MgB_2 samples sintered at different conditions

Sintering condition		Intensity fraction (%)			Lattice parameters (Å)		Goodness of Fit (GOF)
Temperature (°C)	Time (h)	MgB_2 (ICSD: 98-010-6149)	MgO (ICSD: 98-009-4096)	Mg (ICSD: 98–005-1521)	a-axis	c-axis	
700	1	95.9	4.1	–	3.0855 ± 0.0002	3.5239 ± 0.0002	3.11
	3	92.9	5.6	1.5	3.0866 ± 0.0001	3.5231 ± 0.0002	5.50
	7	96.2	3.8	–	3.0852 ± 0.0001	3.5231 ± 0.0002	3.78
1000	1	75.4	24.6	–	3.0832 ± 0.0002	3.5230 ± 0.0003	5.29

residual unreacted Mg in the samples and decomposition of MgB_2, which were the reason for the build-up of Mg vapor inside the sealed stainless steel tubes.

For the ex situ MgB_2 samples with the addition of Mg and sintered at 700 °C for 1–7 h, the a-axis values are slightly smaller compared with the samples without the addition of Mg (Tables 1 & 2). The sample sintered at 1000 °C for 1 h has the smallest a-axis. Nevertheless, the addition of Mg also resulted in a smaller change in the c-axis compared to those without Mg addition. Previously, it was reported that the in situ MgB_2 prepared without excess Mg showed a larger c-axis [36, 37]. As shown in Table 2, prolonged sintering time of 7 h at 700 °C reduced the formation of the MgO phase compared to the samples without the addition of Mg [38], suggesting that the addition of Mg suppressed the decomposition of MgB_2 into MgB_4 and Mg. For the sample sintered at the higher temperature of 1000 °C for 1 h, reaction

kinetics for oxidation of Mg was accelerated, leading to the formation of a large fraction of MgO (24.6%).

The crystallite size of the samples was calculated using the Scherrer equation [39]:

$$L = \frac{K\lambda}{B_{size} \cos \theta} \quad (4)$$

where L is the crystallite size, K is a dimensionless shape factor (0.9), B_{size} is the line broadening at half of the maximum intensity (FWHM) in radian, λ is the X-ray wavelength for $Cu-K_\alpha$ radiation (1.5406 Å), and θ is the Bragg angle in degree. The calculation was made based on the four XRD peaks of (1 0 0), (1 0 1), (0 0 2), and (1 1 0). The average values of the crystallite size are given in Table 3 and Table 4. The increasing sintering temperature for the ex situ MgB_2 samples from 600 °C to 900 °C for 1 h decreased the average crystallite size of the unsintered sample from 52 to 48 nm (Table 3). The reduction in the average crystallite size could be associated with Mg deficiency due to the increased sintering temperature

Table 3 Crystallite size of the samples based on the peaks (1 0 0), (1 0 1), (0 0 2), (1 1 0), average crystallite size, and average grain size for ex situ MgB_2 samples sintered at different conditions

Sintering condition		Crystallite size (nm)					Average grain size, D (µm)
Temperature (°C)	Time (h)	(1 0 0)	(1 0 1)	(0 0 2)	(1 1 0)	Average	
Unsintered	–	57.3	48.0	49.8	51.7	51.7	–
600	1	57.3	48.1	42.1	51.7	49.8	0.55 ± 0.01
700	1	57.3	40.6	49.8	51.7	49.8	0.50 ± 0.02
	3	57.3	40.6	36.5	51.7	46.5	0.51 ± 0.02
	7	73.8	48.1	49.8	51.7	55.8	0.53 ± 0.02
900	1	57.3	40.6	42.1	51.7	47.9	0.50 ± 0.02

Related data for the unsintered ex situ MgB_2 powder (labeled as Unsintered) is included for comparison

Table 4 Crystallite size of the samples based on the peaks (1 0 0), (1 0 1), (0 0 2), (1 1 0), average crystallite size, and average grain size for 0.5 mol Mg added ex situ MgB_2 samples sintered at different conditions

Sintering condition		Crystallite size (nm)					Average grain size, D (µm)
Temperature (°C)	Time (h)	(1 0 0)	(1 0 1)	(0 0 2)	(1 1 0)	Average	
700	1	73.8	48.1	36.5	63.3	55.4	0.26 ± 0.01
	3	57.3	40.6	42.1	51.7	47.9	0.19 ± 0.01
	7	57.3	40.6	36.5	51.7	46.5	0.29 ± 0.01
1000	1	73.8	48.1	42.1	63.3	56.8	0.17 ± 0.01

leading to evaporation of residual unreacted Mg in the samples, as supported by the formation of MgB_4 (Table 1). Except for the sample sintered for 7 h, the prolonged sintering time at 700 °C was expected to decrease the crystallite size compared to that of the unsintered ex situ powder. It is unclear if the larger crystallite size of the sample sintered at 700 °C for 7 h is related to the formation of a high fraction of MgO (37.0%). For the samples with the addition of Mg, sintering at 700 °C and 1000 °C for 1 h increased the average crystallite size relative to that of the unsintered ex situ MgB_2 powder (Table 4) suggesting the crystal growth could be aided by the added Mg. With prolonged sintering time, the average crystallite size of the samples (3 h and 7 h for 700 °C) decreased probably due to the same reason as discussed before (evaporation of a significant amount of Mg).

3.2 Microstructure analysis

Figure 3 shows SEM images of the fractured surfaces of the ex situ MgB_2 bulks. All samples show randomly oriented grains with irregular shapes. Table 3 shows that the average grain size of the *ex situ* MgB_2

decreases slightly only from 0.55 µm to 0.50 µm with the increase of sintering temperature from 600 °C to 900 °C. The trend of change for the grain size is almost similar to that of the crystallite size (Table 3). The slight change in the grain size agrees with the previous finding [14]. Decreasing grain size means increasing the number of grain boundaries for flux pinning to increase J_c [40–42]. The average grain size increased slightly (0.50–0.53 µm), and more voids between grains could be observed clearly with the prolonged sintering time from 1 h (Fig. 3b) to 7 h (Fig. 3d). It is expected the voids will obstruct the current flow between grains and consequently lower the value of J_c [43, 44].

SEM images of Fig. 4 show that the randomly oriented and aggregated grains of the Mg added *ex situ* samples are different from those without the addition of Mg (Fig. 3). The aggregation of the grains may be due to the melting of the added Mg (melting point of Mg is around 650 °C). The melted Mg may play a crucial role in healing the microcracks and enhancing the grain connectivity of the samples [19–21]. By comparing Tables 3 and 4, it is clear that the addition of Mg decreased the average grain size of the samples
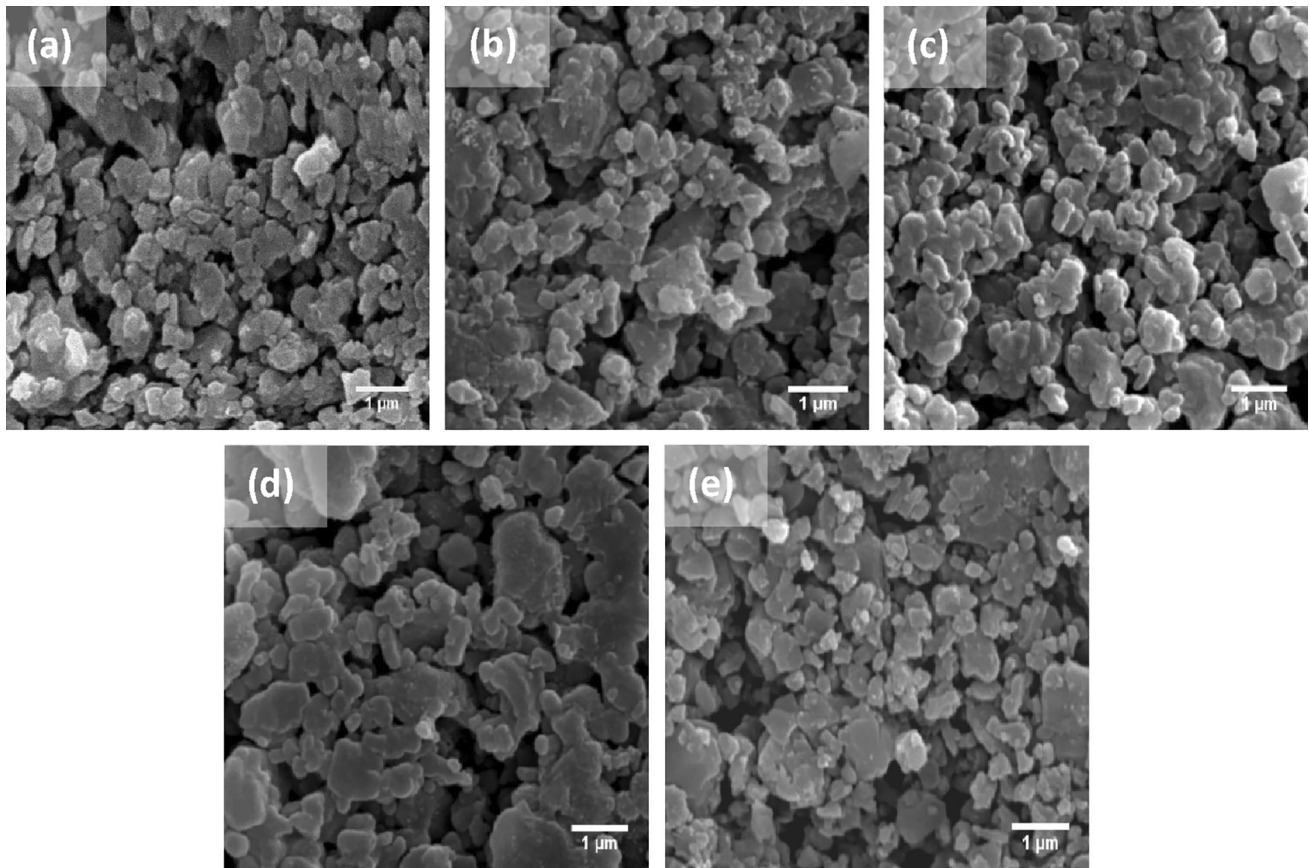
Fig. 3 SEM images of fractured surfaces of ex situ MgB_2 bulks sintered at different conditions: **a** 600 °C, 1 h **b** 700 °C, 1 h **c** 700 °C, 3 h **d** 700 °C, 7 h, and **e** 900 °C, 1 h

by about 50% or more. A previous study suggested that excess Mg reduced the grain size of the in situ MgB_2 attributable to the formation of more MgB_2 nucleation seeds [19]. For the samples sintered at 700 °C, the average grain size varied between 0.19 and 0.29 μm. The average grain size of the samples sintered for 1 h decreased from 0.26 to 0.17 μm upon increasing the sintering temperature from 700 to 1000 °C. The variation in the average grain size (Table 4) is actually due to two reasons. First of all, the added Mg powders may act as seeds for the growth of more MgB_2 grains with smaller sizes in the range of 0.05–0.15 μm [19]. Secondly, significant grain growth leading to bigger grains during the sintering did not occur, consistent with previous findings [14]. Nevertheless, fewer grains with the size of 0.45–0. 65 μm was observed from the SEM images. For the Mg added samples sintered at 700 °C for 3 h and 1000 °C for 1 h, their average grain size is 19 ± 0.01 μm and 17 ± 0.01 μm, respectively. In these samples, SEM images showed the presence of more grains with smaller sizes (0.05–0.15 μm) than the bigger ones (0.45–0. 65 μm). Consequently, the average value of the grain size became smaller.

3.3 Superconducting properties

Figure 5 shows field dependence of J_c at 20 K for all the samples. As the sintering temperature increased from 600 to 900 °C, the self-field J_c at 20 K for the ex situ MgB_2 increased from 1.8 to 4.2 kA cm^{-2} (Table 5). The value of self-field J_c increased abruptly with the addition of Mg into the *ex situ* MgB_2 samples (Table 6). As the sintering temperature was increased to 1000 °C, self-field J_c at 20 K was increased to 39.8 kA cm^{-2}, a value more than 20 times larger than that of the ex situ sample without the addition of Mg sintered at 600 °C for 1 h (1.8 kA cm^{-2}). The main reason for the increased J_c is the improved grain coupling due to higher sintering temperature and the addition of Mg [14, 21]. The highest J_c for the ex situ samples and that added with Mg sintered at 900 °C

Fig. 4 SEM images of fractured surfaces of 0.5 mol Mg added ex situ MgB_2 bulks sintered at 700 °C for **a** 1 h **b** 3 h **c** 7 h, respectively, and **d** 1000 °C for 1 h
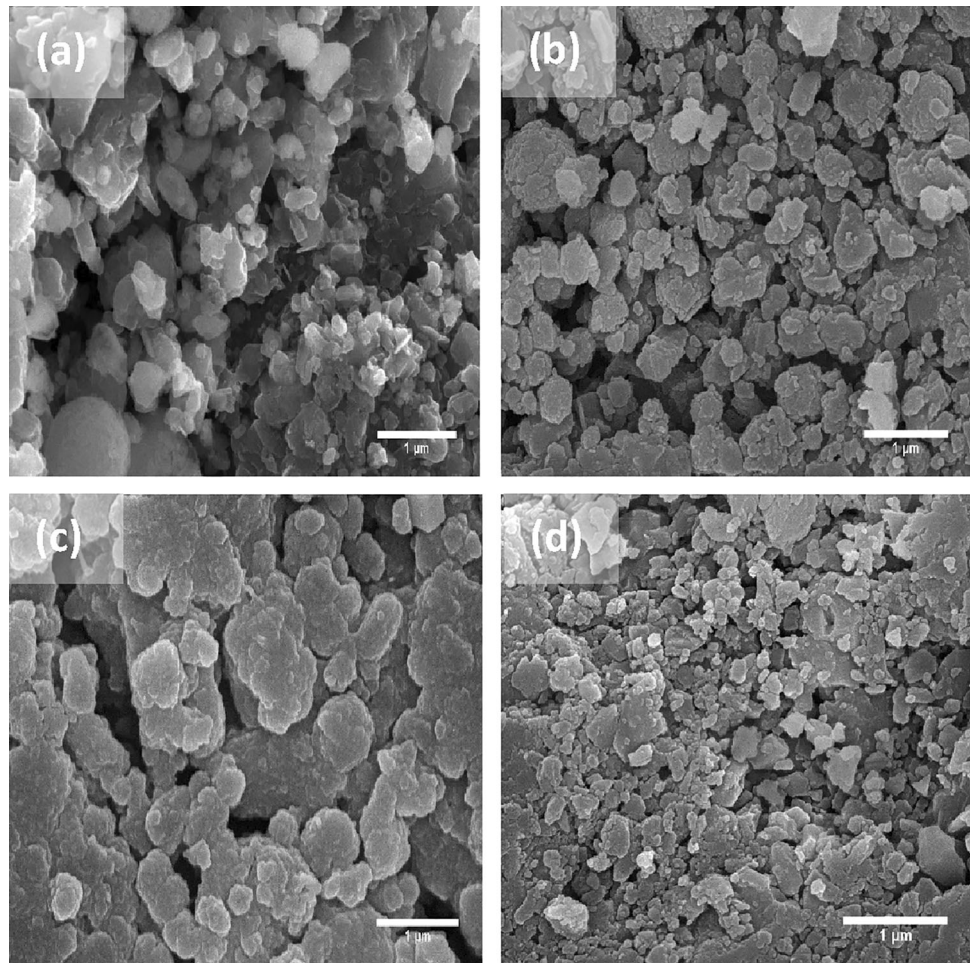

and 1000 °C, respectively, is consistent with the occurrence of solid-state self-sintering [14]. Consequently, grain coupling is further strengthened by forming necks between the adjacent grains [14].

As a result of increasing the sintering time to 3 h at 700 °C, J_c (0 T, 20 K) of the ex situ MgB_2 and that with the addition of Mg increased to 3.2 kA cm^{-2} and 18.4 kA cm^{-2}, respectively. However, these values decreased to 0.5 kA cm^{-2} and 13.2 kA cm^{-2}, respectively, as the sintering time was prolonged to 7 h. The drastic decrease in J_c of the former may be due to the large fraction of MgO (37%) in the sample (Table 1). As discussed in Sect. 3.2, the presence of more voids may also be part of the reason for the lower J_c in the ex situ MgB_2 samples (Fig. 5a).

For the same heat treatment at 700 °C for 1 h with the addition of Mg, self-field J_c (20 K) of our ex situ sample is 6.3 kA cm^{-2} (Table 6) as compared with 20 kA cm^{-2} for the ex situ MgB_2 reported by Wu [21]. The lower J_c of our sample is attributed to the addition of excessive Mg (0.5 mol as compared with 0.1 mol in [21]), causing inhomogeneity in the sample as shown by the double-step transition in Fig. 6b. Nevertheless, self-field J_c (20 K) of our Mg added sample sintered at 700 °C for 3 h is close to that obtained by Wu [21]. For homemade ex situ MgB_2 sintered at 900 °C for a much longer 48 h [14], its self-field J_c at 20 K is 3.1×10^5 A cm^{-2}. Taken all, sintering with Mg addition provides a window of opportunity for enhancing J_c of ex situ MgB_2 at lower temperature and shorter time. It is anticipated that J_c of our Mg added ex situ sample sintered at 1000 °C for 1 h could be increased further by reducing its MgO fraction and further optimizing heat treatment conditions.

Figure 6 shows that all the samples have a very similar onset of critical temperature, $T_{c\text{-onset}}$, which is about 38.5 K. $T_{c\text{-onset}}$ of the sample with the addition of Mg and sintered at 1000 °C for 1 h has a relatively smaller T_c of 38.1 K (Table 6). Such a slight variation
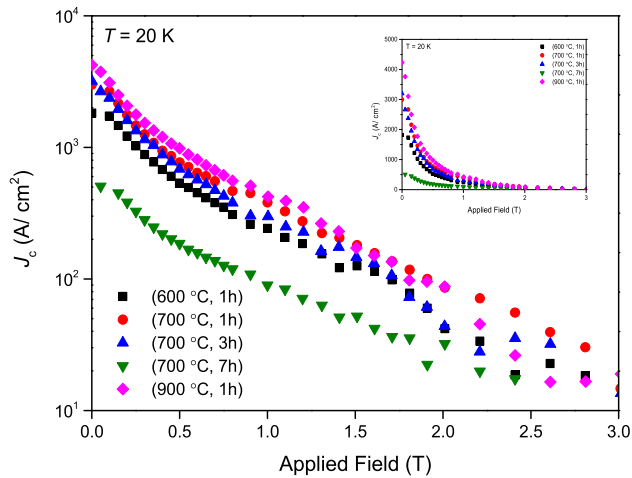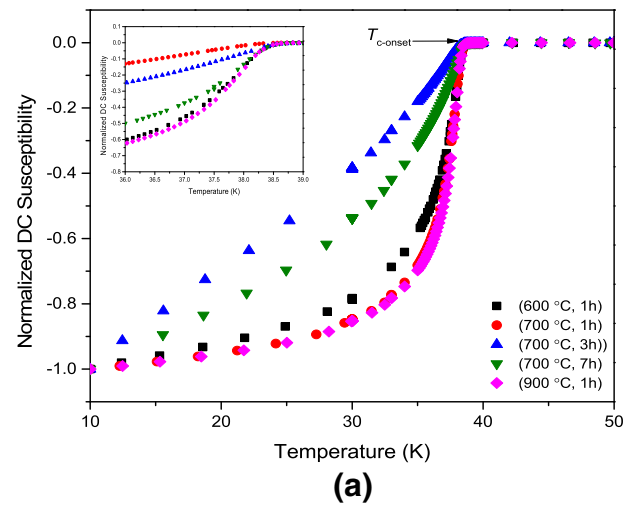
(a)
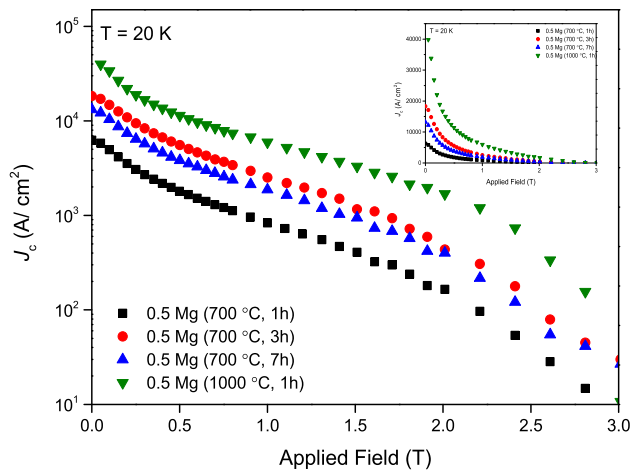
(b)

Fig. 5 Field dependence of critical current density, J_c (20 K) in logarithmic scale for **a** ex situ MgB$_2$ and **b** 0.5 mol Mg added ex situ MgB$_2$ sintered at different conditions. Insets show the same plots of field dependence of J_c in linear scale

Table 5 Onset of critical temperature, $T_{c\text{-onset}}$, and critical current density, J_c at 0 T, 20 K for ex situ MgB$_2$ samples sintered at different conditions

Sintering condition		$T_{c\text{-onset}}$ (K)	J_c (A cm^{-2})
Temperature (°C)	Time (h)		
600	1	38.5	1.8×10^3
700	1	38.5	3.0×10^3
	3	38.5	3.2×10^3
	7	38.5	0.5×10^3
900	1	38.5	4.2×10^3

Table 6 Onset of critical temperature, $T_{c\text{-onset}}$, and critical current density, J_c at 0 T, 20 K for 0.5 mol Mg added ex situ MgB$_2$ samples sintered at different conditions

Sintering condition		$T_{c\text{-onset}}$ (K)	J_c (A cm^{-2})
Temperature (°C)	Time (h)		
700	1	38.5	6.3×10^3
	3	38.5	18.4×10^3
	7	38.5	13.2×10^3
1000	1	38.1	39.8×10^3

(a)
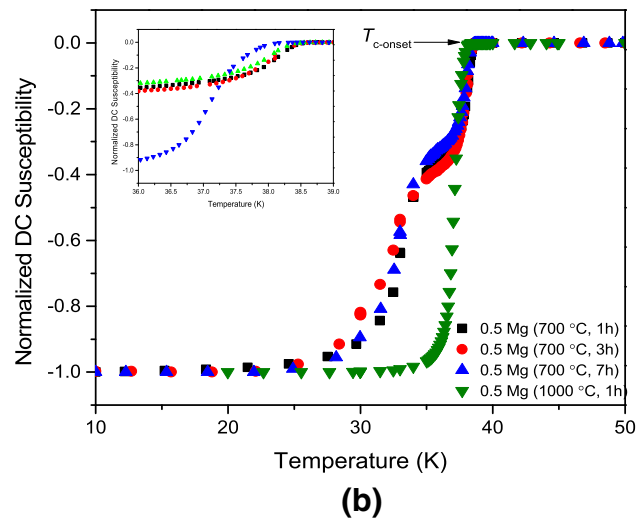
(b)

Fig. 6 Temperature dependence of normalized DC susceptibility for **a** ex situ MgB$_2$ and **b** 0.5 mol Mg added ex situ MgB$_2$ sintered at different conditions. Insets show the same plots of temperature dependence of normalized DC susceptibility fora temperature range from 36 K to 39 K. $T_{c\text{-onset}}$ was determined by taking the first deviation point from linearity that signifies the transition from the normal to superconducting state

in $T_{c\text{-onset}}$ across the samples is consistent with previous findings [21], indicating Mg addition did not change the electronic structure of MgB_2 [45]. Instead, Mg addition promoted self-sintering by enhancing the grain coupling [21] and suppressed decomposition of MgB_2 (as shown by the XRD data). With the addition of Mg, a double-step transition for the samples sintered at 700 °C was observed (Fig. 6b). The superconductor transition width, ΔT, broadened as the sintering time increased from 1 to 7 h. The broadening of ΔT together with the double-step transition indicates inhomogeneity within the samples [46]. For the sample sintered at 1000 °C for 1 h, a single-step transition was observed consistent with the higher J_c in this sample due to better grain connectivity.

For phase pure MgB_2 samples with well-connected grains (phase coherence), intergranular T_c and J_c are close to the intragranular ones [47]. Depending on the degree of grain coupling and the nature of impurities, grain boundaries may either reduce the effective area for current transport (if they are entirely insulating) or behave like Josephson junctions [48]. As a result, intergranular J_c is expected to be lower than intragranular one. This scenario is especially true for the samples with a significant fraction of impurities and insufficient sintering (Tables 1 and 2). As discussed before, J_c of the Mg added sample sintered at 1000 °C is the highest because of enhanced grain coupling due to solid-state self-sintering, which occurred at higher temperature [14] despite its high fraction of MgO. While the intragrain T_c should remain unchanged concerning the heat treatment [38], the double-step transition (Fig. 6b) may be caused by the presence of Josephson junctions due to the inhomogeneity in the samples.

4 Conclusion

We have demonstrated the effect of Mg addition for sintering on the superconducting properties of ex situ MgB_2. The addition of Mg increased the partial pressure of Mg and suppressed the decomposition of MgB_2 into MgB_4 and Mg. As estimated from the SEM images, the average grain size of the Mg added

samples are smaller. While the T_c of those samples remained unchanged at ~ 38 K, their J_c was enhanced by more than 20 times as the sintering temperature was increased. For the sintering carried out for 1 h, J_c increased to $\sim 4 \times 10^4$ A cm^{-2} for the sample added with Mg and sintered at 1000 °C. This work shows that short sintering with the aid of Mg is effective for grain coupling leading to enhanced J_c of ex situ MgB_2.

Research data policy and data availability statements

The datasets generated during and/or analyzed during the current study are not publicly available due to the reasons of ethics and ownership, but are available from the corresponding author on reasonable request.

Declarations

Conflict of interest The authors declare no conflict of interest among themselves.

References

1. J. Nagamatsu, N. Nakagawa, T. Muranaka, Y. Zenitani, J. Akimitsu, Nature **410**, 63–64 (2001)

2. B. Cristina, Y. Tsutomu, Supercond. Sci. Technol. **14**, R115–R146 (2001)

3. A. Yamamoto, H. Tanaka, J.I. Shimoyama, H. Ogino, K. Kishio, T. Matsushita, Jpn. J. Appl. Phys. **51**, 010105 (2012)

4. A. Ballarino, R. Flükiger, J. Phys. Conf. Ser. **871**, 012098 (2017)

5. K. Vinod, R.G. Abhilash Kumar, U. Syamaprasad, Supercond. Sci. Technol. **20**, R1–R13 (2007)

6. M. Tomsic, M. Rindfleisch, J. Yue, K. McFadden, J. Phillips, Appl. Ceram. Technol. **4**, 250–259 (2007)

7. J.P.F. Feighan, A. Kursumovic, J.L. MacManus-Driscoll, Supercond. Sci. Technol. **30**, 123001 (2017)

8. N.M. Hapipi, S.K. Chen, A.S. Halim, M.M. Awang Kechik, K.B. Tan, K.P. Lim, O.J. Lee, J. Supercond. Nov. Magn. **32**, 1191–1198 (2019)

9. A. Yamamoto, J.I. Shimoyama, K. Kishio, T. Matsushita, Supercond. Sci. Technol. **20**, 658–666 (2007)

10. M. Muralidhar, M. Higuchi, M. Jirsa, P. Diko, I. Kokal, M. Murakami, IEEE Trans. Appl. Supercond. **27**, 6201104 (2017)

11. S.S. Arvapalli, M. Miryala, M. Murakami, J. Supercond. Nov. Magn. **32**, 1891–1895 (2019)

12. J.H. Kim, S.X. Dou, J.L. Wang, D.Q. Shi, X. Xu, M.S.A. Hossain, Supercond. Sci. Technol. **20**, 448–451 (2007)

13. G. Zhao-Shun, M. Yan-Wei, W. Dong-Liang, Z. Xian-Ping, A. Satoshi, W. Kazuo, Chin. Phys. Lett. **27**, 111 (2010)

14. H. Tanaka, A. Yamamoto, J.I. Shimoyama, H. Ogino, K. Kishio, Supercond. Sci. Technol. **25**, 117401 (2012)

15. S. Mizutani, A. Yamamoto, J.I. Shimoyama, H. Ogino, K. Kishio, Supercond. Sci. Technol. **27**, 114001 (2014)

16. A. Malagoli, V. Braccini, C. Bernini, G. Romano, M. Vignolo, M. Putti, C. Ferdeghini, Supercond. Sci. Technol. **23**, 025032 (2010)

17. Y. Shimada, S. Hata, K. Ikeda, H. Nakashima, S. Matsumura, H. Tanaka, A. Yamamoto, J. Shimoyama, K. Kishio, J. Alloys Compd. **656**, 172–180 (2016)

18. H. Kobayashi, M. Muralidhar, M.R. Koblischka, K. Inoue, M. Murakami, Phys. Procedia **65**, 73–76 (2015)

19. R. Zeng, L. Lu, W.X. Li, J.L. Wang, D.Q. Shi, J. Horvat, S.X. Dou, M. Bhatia, M. Sumption, E.W. Collings, J.M. Yoo, M. Tomsic, M. Rindfleisch, J. Appl. Phys. **103**, 083911 (2008)

20. H. Zhang, Y. Zhao, Y. Zhang, J. Supercond. Nov. Magn. **28**, 2711–2714 (2015)

21. F. Wu, J. Low Temp. Phys. **177**, 157–164 (2014)

22. K.L. Tan, K.P. Lim, A.S. Halim, S.K. Chen, Phys. Status Solidi A **210**, 616–622 (2013)

23. D.X. Chen, R.B. Goldfarb, J. Appl. Phys. **66**, 2489–2500 (1989)

24. M. Muralidhar, N. Kenta, M.R. Koblischka, M. Murakami, Phys. Status Solidi A **212**, 2141–2145 (2015)

25. Y. Guo, W. Zhang, D. Yang, R.L. Yao, J. Am. Ceram. Soc. **95**, 754–759 (2012)

26. G. Balducci, S. Brutti, A. Ciccioli, G. Gigli, P. Manfrinetti, A. Palenzona, M.F. Butman, L. Kudin, J. Phys. Chem. Solids **66**, 292–297 (2005)

27. J. Peng, Q. Cai, F. Cheng, Z. Ma, C. Li, Y. Xin, Y. Liu, J. Alloys Compd. **694**, 24–29 (2017)

28. T. Degen, M. Sadki, E. Bron, U. König, G. Nénert, Powder Diffr. **29**, S13–S18 (2014)

29. S.K. Chen, A. Serquis, G. Serrano, K.A. Yates, M.G. Blamire, D. Guthrie, J. Cooper, H. Wang, S. Margadonna, J.L. MacManus-Driscoll, Adv. Funct. Mater. **18**, 113–120 (2008)

30. J.H. Kim, S.X. Dou, D.Q. Shi, M. Rindfleisch, M. Tomsic, Supercond. Sci. Technol. **20**, 1026–1031 (2007)

31. K.Y. Tan, K.L. Tan, K.B. Tan, K.P. Lim, S.A. Halim, S.K. Chen, J. Supercond. Nov. Magn. **24**, 2025–2029 (2011)

32. N.M. Hapipi, M. Miryala, S.K. Chen, S.S. Arvapalli, M. Murakami, M.M. Awang Kechik, K.B. Tan, O.J. Lee, Ceram. Int. **46**, 23041–23048 (2020)

33. G. Balducci, S. Brutti, A. Ciccioli, G. Gigli, P. Manfrinetti, A. Palenzona, M.F. Butman, L. Kudin, J. Phys. Chem. Solids. **66**, 292–297 (2005)

34. K.L. Tan, K.Y. Tan, K.P. Lim, A.H. Shaari, S.K. Chen, J. Electron. Mater. **41**, 673–678 (2012)

35. R. Schmitt, J. Glaser, T. Wenzel, K.G. Nickel, H.J. Meyer, Phys. C **436**, 38–42 (2006)

36. S.K. Chen, K.A. Yates, M.G. Blamire, J.L. MacManus-Driscoll, Supercond. Sci. Technol. **18**, 1473–1477 (2005)

37. W. Mickelson, J. Cumings, W.Q. Han, A. Zettl, Phys. Rev. B **65**, 052505 (2002)

38. A. Gupta, A. Kumar, A.V. Narlikar, Supercond. Sci. Technol. **22**, 105005 (2009)

39. J.I. Langford, A.J.C. Wilson, J. Appl. Cryst. **11**, 102–113 (1978)

40. Z. Gao, Y. Ma, D. Wang, X. Zhang, IEEE Trans. Appl. Supercond. **20**, 1515–1520 (2010)

41. S.G. Jung, W.K. Seong, W.N. Kang, J. Appl. Phys. **111**, 053906 (2012)

42. G. Giunchi, G. Ripamonti, S. Raineri, D. Botta, R. Gerbaldo, R. Quarantiello, Supercond. Sci. Technol. **17**, S583–S588 (2004)

43. E.W. Collings, M.D. Sumption, M. Bhatia, M.A. Susner, S.D. Bohnenstiehl, Supercond. Sci. Technol. **21**, 103001 (2008)

44. M. Shahabuddin, N.S. Alzayed, S. Oh, S. Choi, M. Maeda, S. Hata, Y. Shimada, M.S.A. Hossain, J.H. Kim, AIP Adv. **4**, 017113 (2014)

45. J. Kortus, O.V. Dolgov, R.K. Kremer, A.A. Golubov, Phys. Rev. Lett. **94**, 1–4 (2005)

46. W.X. Li, R. Zeng, J.L. Wang, Y. Li, S.X. Dou, J. Appl. Phys. **111**, 07E135 (2012)

47. M. Dhallé, P. Toulemonde, C. Beneduce, N. Musolino, M. Decroux, R. Flükiger, Phys. C **363**, 155–165 (2001)

48. J.M. Rowell, Supercond. Sci. Technol. **16**, R17–R27 (2003)